Electronic Supplementary Information (ESI)

Synchronous achievement of ultra-wideband microwave absorption and high thermal conduction in spongy TiO_2-based magnetic composites via constructing magnetic/dielectric double loss and phonon/electron co-transmission

Qibin Yao[†], Kang Fu[†], Ran Ji[†], Meiwan Ying[†], Yijun Yang[†], Kaixia Yang[†], Guoxiu Tong[*†‡], Wenhua Wu[†] and Dabo Chen[*‡§]

[†]*College of Chemistry and Materials Sciences, Key Laboratory of the Ministry of Education for Advanced Catalysis Materials, Zhejiang Normal University, Jinhua 321004, People's Republic of China*

[‡]*Zhejiang Hanzao intelligent Technology Co., LTD, Quzhou 324400, China.*

[§]*The College of Electrical and Information Engineering, Hunan University, Changsha 410082, China.*

*Corresponding Authors: E-mail: tonggx@zjnu.cn (G.X. Tong). China bc@newmorex.com (D.B. Chen); Tel.: +86-579-82282269; Fax: +86-579-82282269.

Experiment section

Characterization

ZEISS GeminiSEM 300 scanning electron microscope (SEM, 10 kV) and a Horiba EX-250 energy dispersive X-ray spectrometer (EDS) connected with it were applied to analyze the surface morphology, element content and distribution of the spongy TiO_2-based magnetic composites. A software (named Nano Measurer) was used to measure the diameters of the nanoparticles. A JEM-2100F transmission electron microscope (TEM, 200 kV) was used to further confirm the microstructure of products. A D/MAX-IIIA X-ray diffractometer (XRD) with X-ray (λ = 0.15418 nm, came from Cu Kα) as the

radiation source was employed to record XRD patterns for the phase analysis. The working voltage, working current, and scanning speed were 40.0 kV, 40.0 mA, 6 °/min, respectively. The crystallite sizes and the microstrain level were obtained by analyzing and calculating using jade 6. The mean crystal size (D) values of the samples calculated using the Hall–Williamson equation: $\beta \cos\vartheta = k\lambda/\delta + 2\varepsilon \sin\vartheta$, where β is the full width at half-maximum (FWHM) of the samples, λ is the x-ray wave length used, δ is the grain size, k is the Scherer constant, ε is the internal strain, and ϑ is the Bragg angle. β can be written as $\beta^2 = \beta^2_{exp} - \beta^2_{inst}$, where β_{inst} is the FWHM of Si powder used for calibration and β_{exp} is the evaluated FWHM.

Fourier transform infrared (FTIR) spectroscopy obtained in the transmission mode within the scanning range from 400 to 4000 cm^{-1} was used to evaluate the surface functionalities of the spongy TiO_2-based magnetic composites, using a Nicolet 8700 Fourier transform infrared spectrometer.

The graphitization degree analysis of carbon was executed on a Renishaw RM10000 Raman spectrometer. The oxidation states of surface elements are assessed in the samples using a ESCALAB250 X-ray photoelectron spectroscopy (XPS). To obtain the Brunauer–Emmett–Teller (BET) specific surface area (S_{BET}), the N_2 adsorption/desorption isotherm was done on an Autosorb iQ instrument (Quantachrome, Florida, USA), and the sample was outgassed under vacuum at 160 °C for 8 h.

Measurement of conductivity, EM parameters, and heat conductance.

The conductivity of the prepared the spongy TiO_2-based magnetic composites was evaluated by A four-point probe (RTS-9 model) method. To measure the conductivity, the disc pellets about 7 mm in diameter and 1.0 mm in thickness were formed by pressing the spongy TiO_2-based magnetic composites in a mold.

The as-obtained spongy TiO_2-based magnetic composites were mixed uniformly with molten paraffin in equal amounts (1:1, m/m), and the standard toroidal-shaped specimens were prepared with a mold to determine the EMWAPs. The thickness, outer diameter, and inner diameter of the standardized specimens were ca. 3.5 mm, 7.0 mm, and 3.04 mm, respectively. With the coaxial line method adopted, the permeability ($\mu_r = \mu' - j\mu''$) and permittivity ($\varepsilon_r = \varepsilon' - j\varepsilon''$) were measured using a Keysight

N5230A vector network analyzer. Reflection loss (*RL*) generally representing the EMWAPs are computed by the equation: $RL = 20\log\left|\frac{\sqrt{\mu_r/\varepsilon_r}\tanh[j(2\pi fd/c)\sqrt{\mu_r\varepsilon_r}]-1}{\sqrt{\mu_r/\varepsilon_r}\tanh[j(2\pi fd/c)\sqrt{\mu_r\varepsilon_r}]+1}\right|$, where *f, c,* and *d,* correspond to the frequency, light velocity under vacuum, sample thickness, respectively. The attenuation constant (*A*) and matching constant (*Z*) are computed based on the formula: $A=\frac{\sqrt{2}\pi f}{c}\sqrt{(\mu''\varepsilon''-\mu'\varepsilon')+\sqrt{(\mu'\varepsilon''+\mu''\varepsilon')^2+(\mu''\varepsilon''-\mu'\varepsilon')^2}}$ and $Z=\left|\frac{Z_{in}}{Z_0}\right|=\left|\sqrt{\frac{\mu_r}{\varepsilon_r}}\tanh\left(j\frac{2\pi fd}{c}\sqrt{\mu_r\varepsilon_r}\right)\right|$, respectively.

Using a transient plane source (TPS) thermal characterization technique with a Hot Disk Thermal Constant Analyzer TPS 2500 apparatus which meets the ISO Standard 22007e2, the thermal conductivity of the spongy TiO_2-based magnetic composites was analyzed. When performing a measurement, a plane Hot Disk sensor of 5465 is fitted between two pieces of the sample, each one with a plane surface facing the sensor which is used both as a heat source and as a dynamic temperature sensor. By running an electrical current, the temperature of the sensor increases, and the resistance (temperature) increase as a function of time was recorded at the same time to obtain the thermal conductivity. All measurements were carried out at room temperature and the average value of three repeated tests was determined.

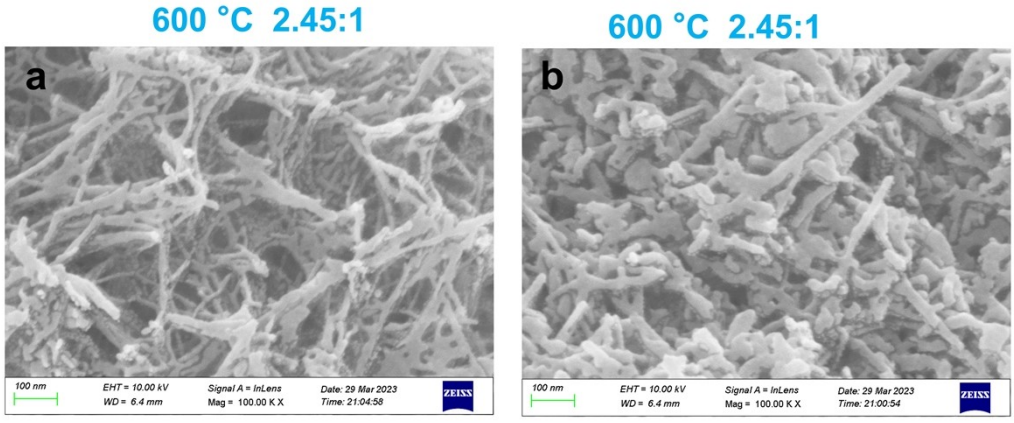

Fig. S1. SEM images of (a) TiO_2@$CoTiO_3$@Co@C and (b) TiO_2@Ni@C composites formed at 600°C.

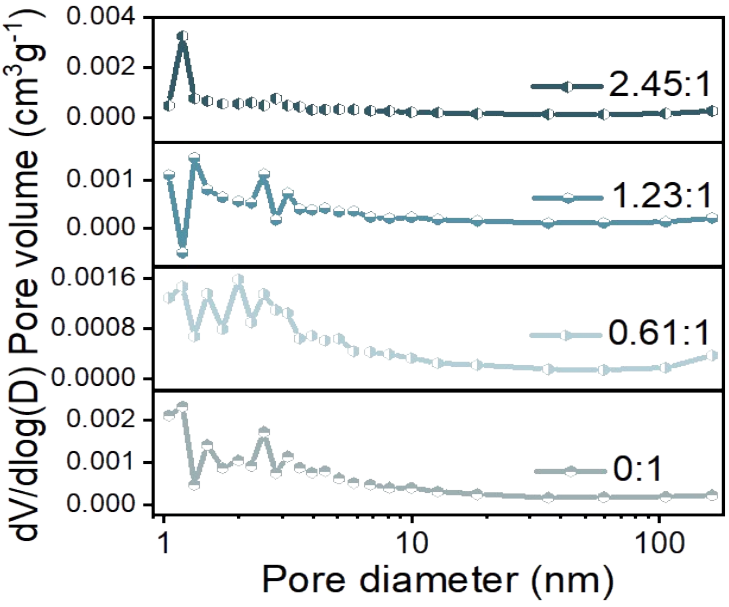

Fig. S2. pore size distribution plots of TiO_2@Ni@C composites formed under various Ni^{2+}/Ti^{4+} molar ratios (φ).

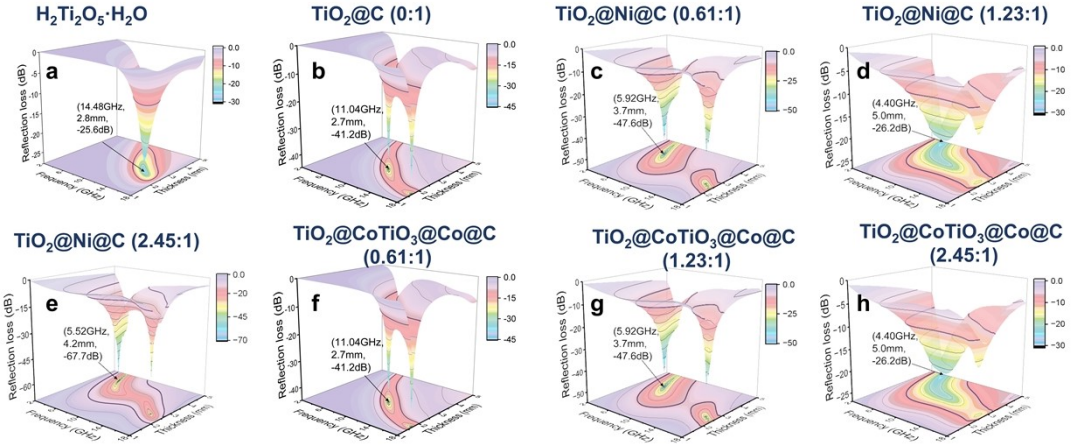

Fig. S3. Frequency features: (a–h) 3D RL plots of $H_2Ti_2O_5·H_2O$ nanotubes, TiO_2@C, TiO_2@Ni@C, TiO_2@$CoTiO_3$@Co@C composites formed under various φ.

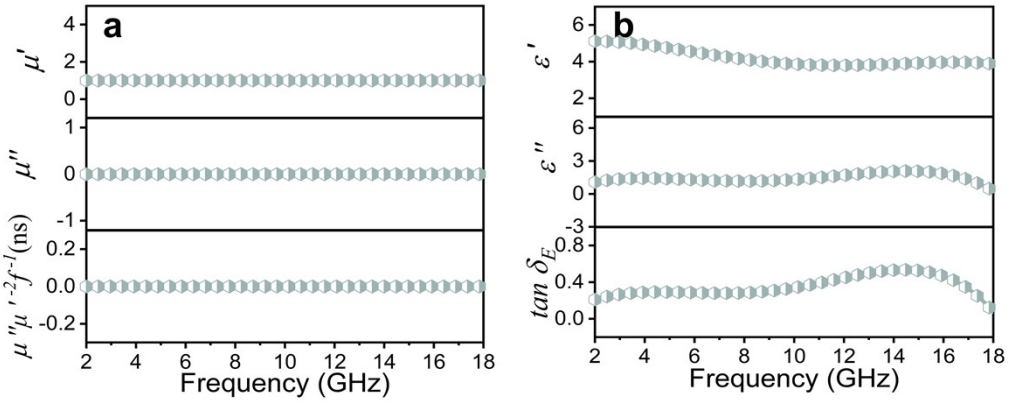

Fig. S4. (a) The real part (μ') and imaginary part (μ'') of relative complex permeability, and eddy current loss (denoted by $\mu''(\mu')^{-2}f^{-1}$); (b) The real part (ε') and imaginary part (ε'') of relative complex permittivity and dielectric loss ($\tan\delta_E$) for $H_2Ti_2O_5{\cdot}H_2O$ nanotubes.

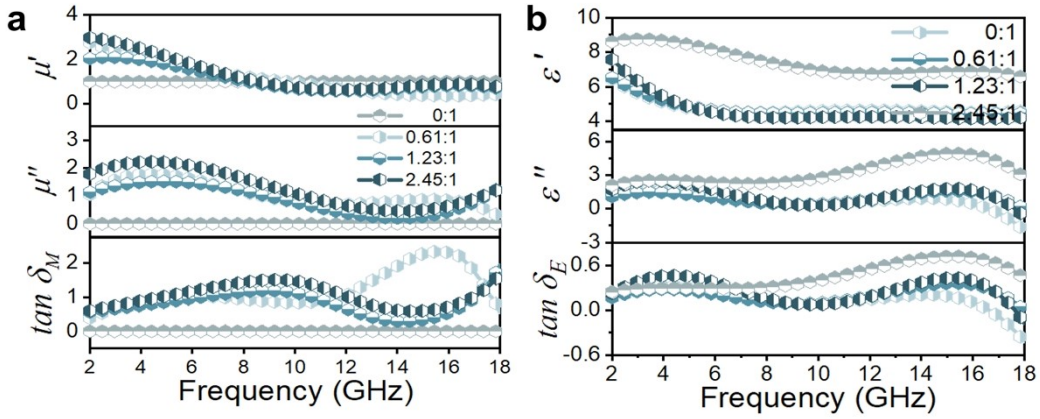

Fig. S5. (a) The real part (μ') and imaginary part (μ'') of relative complex permeability, and magnetic loss ($\tan\delta_M$); (b) The real part (ε') and imaginary part (ε'') of relative complex permittivity and dielectric loss ($\tan\delta_E$) for TiO_2@Ni@C composites formed under various φ.

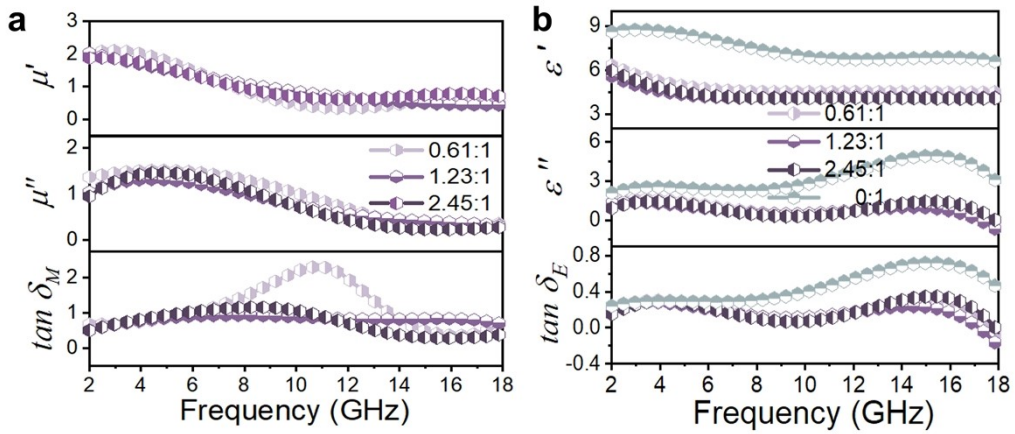

Fig. S6. (a) The real part (μ') and imaginary part (μ'') of relative complex permeability, and magnetic loss ($\tan\delta_M$); (b) The real part (ε') and imaginary part (ε'') of relative complex permittivity and dielectric loss ($\tan\delta_E$) for TiO_2@$CoTiO_3$@Co@C composites formed under various φ.

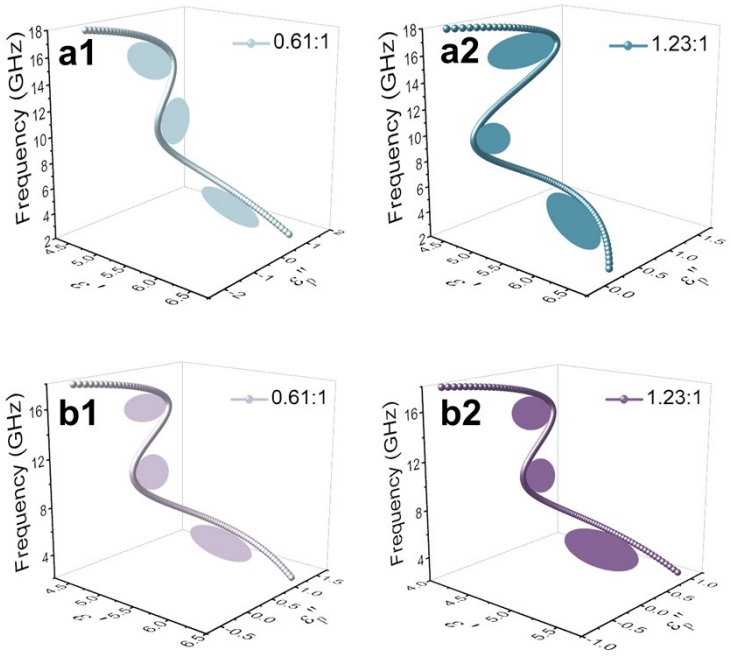

Fig. S7. Cole–Cole plots (ε' versus ε'') of (a1, a2) TiO_2@Ni@C and (b1, b2) TiO_2@$CoTiO_3$@Co@C composites formed under various φ.

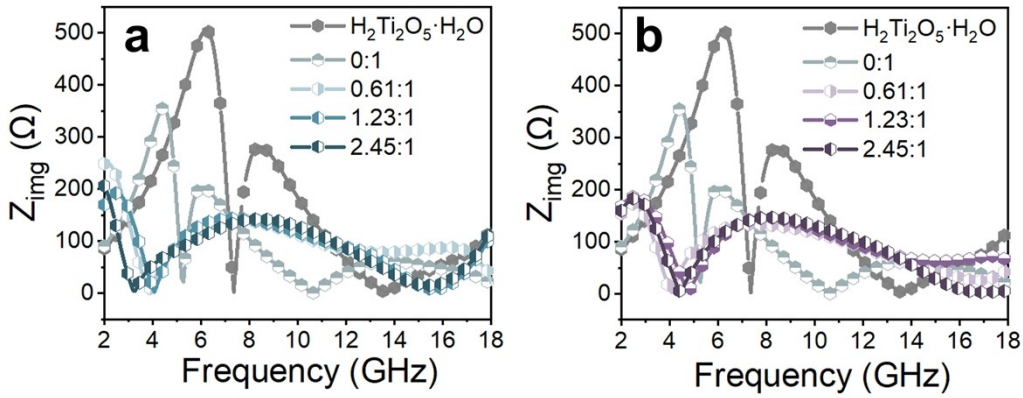

Fig. S8. The imagery part of Z (Z_{img}) of (a) TiO_2@Ni@C and (b) TiO_2@$CoTiO_3$@Co@C composites formed under various φ.

Table S1. A EMWAP comparison of spongy Ti-based composites with other absorbents

Specimens		loading (wt%)	RL_{min} (dB)	*f* (GHz) (optimal R_L)	*d* (mm)	EAB (GHz) (RL ≤–10 dB)	ABW/*d* (GHz/mm)	Ref.
300℃ annealed TiO_2		80	-36.90	14.30	4.00	1.00	0.25	[23]
Ni@TiO_2		70	-35.40	17.80	4.00	1.00	0.25	[39]
TiO_2@C		40	-58.50	7.60	5.50	4.26	0.77	[28]
(CNT)/TiO_2		30	-31.80	10.35	2.00	2.76	1.38	[34]
BFTO/MCNTs/P_3MT		70	-21.56	11.40	2.00	3.25	1.63	[56]
TiO_2/PANI/GO		/	-51.74	9.67	2.50	4.76	1.90	[36]
TiO_2@CZ_24h		40	-42.00	11.50	2.50	5.00	2.00	[57]
TC20		20	-56.20	17.00	5.00	10.00	2.00	[51]
graphene@Fe_3O_4@PANI@TiO_2		50	-41.80	14.40	1.60	3.50	2.19	[37]
C-TiO_2		40	-25.40	/	3.00	6.60	2.20	[58]
Fe/Fe_3O_4@TCNFs@TiO_2		15	-44.80	13.90	1.60	3.70	2.31	[40]
TRGO-1.5		20	-27.20	14.80	2.10	5.20	2.48	[59]
C@TiO_2		40	-49.21	/	2.20	5.50	2.50	[30]
TiO_2/RGO/Fe_2O_3		60	-44.05	14.48	2.00	5.60	2.80	[31]
TiO_2/C		40	-49.60	/	1.60	4.60	2.88	[32]
TiO_2/RGO		20	-42.80	8.72	2.15	6.20	2.88	[33]
Al/H-TiO_2		60	-58.20	6.61	1.61	6.13	3.09	[60]
C/TiO_2/α-Fe		70	-45.10	3.90	1.00	3.30	3.30	[61]
H-A-TiO_2@Ni		50	-64.20	/	2.50	9.50	3.80	[38]
CoNi@SiO_2@TiO_2		/	-58.20	10.40	2.10	8.10	3.86	[43]
Fe_3O_4@TiO_2		/	-33.40	7.00	2.00	7.80	3.90	[44]
Fe_3O_4@black TiO_{2-x}		/	-32.40	15.50	2.90	13.00	4.48	[45]
B-TiO_2/C		50	-73.20	/	1.50	6.80	4.53	[29]
$H_2Ti_2O_5·H_2O$		30	-25.60	14.48	3.00	4.48	1.49	This work
TiO_2@C	0:1	30	-41.20	11.04	2.00	5.44	2.72	
TiO_2@Ni@C composites	0.61:1	30	-49.40	8.16	2.50	9.60	3.84	
	1.23:1	30	-50.30	6.72	2.80	11.92	4.26	
	2.45:1	30	-55.00	5.60	2.60	13.36	5.14	
TiO_2@$CoTiO_3$@Co@C composites	0.61:1	30	-47.60	5.92	2.90	11.44	3.94	
	1.23:1	30	-26.20	4.40	3.30	13.84	4.19	
	2.45:1	30	-67.70	5.52	2.70	12.48	4.62	

Table S2. The TC comparison of 30 wt.% Ti-based composites/silicone films with other fillers

Filler		Loading (wt%)	Heat conductivity (W/m·K)	Ref.
SiC-SiO_2-Al_2O_3-TiO_2		80	0.12	[13]
TiO_2/paraffin/SSL		100	0.22	[11]
Cu_2Se/TiO_2		100	0.35	[12]
Thiolene/TiO_2		90	0.76	[14]
Pt@TiO_2		100	1.00	[15]
porous TiO_2 foam		25	1.06	[65]
TiO_2-Cu NWs		15	1.12	[66]
Al_2O_3/TiO_2		100	1.25	[16]
P123 sol-gel TiO_2		100	1.26	[17]
TiO_2 nanowire		100	1.30	[18]
Ellipsoidal TiO_2		52	1.70	[19]
g-C_3N_4@Fe@C		20	1.81	[67]
TiO_2/Fe/C		45	1.87	[2]
Fe-doped CeO_2/$Ce(OH)_3$		30	2.31	[68]
$Ti_3C_2T_x$		50	2.75	[69]
TiO_2/ZnO		100	2.78	[20]
γ-Al_2O_3@Ni@C		30	2.84	[70]
$H_2Ti_2O_5·H_2O$ nanotubes		30	1.47	
TiO_2@C composites	0:1	30	2.44	
TiO_2@Ni@C composites	0.61:1	30	2.99	
	1.23:1	30	3.12	This work
	2.45:1	30	3.38	
TiO_2@$CoTiO_3$@Co@C composites	0.61:1	30	3.08	
	1.23:1	30	3.27	
	2.45:1	30	3.43	